Ionics (2024) 30:1785–1793
https://doi.org/10.1007/s11581-023-05362-8

RESEARCH

Enhanced performance of solar-blind UV detectors based on $Ti_3C_2T_x$/AlGaN heterojunction

Jingzhao Yü[1] · Yuqing Zhang[1] · Liying Wang[1] · Xijia Yang[1] · Yue Yang[1] · Ke Jiang[2] · Wei Lü[1,2] · Xiaojuan Sun[2]

Received: 1 November 2023 / Revised: 3 December 2023 / Accepted: 20 December 2023 / Published online: 3 January 2024

Abstract

AlGaN is an ideal material for fabricating ultraviolet (UV) photodetectors targeting the solar-blind wavelength range. However, the performance of UV detectors based on AlGaN is still limited by its material quality and effective p-type doping. Herein, we propose an external modulation method by combining AlGaN with two-dimensional MXene ($Ti_3C_2T_x$) to construct $Ti_3C_2T_x$/AlGaN heterostructures. It has been shown that $Ti_3C_2T_x$ undergoes a transition from a metallic material to a semiconductor depending on oxidation, and the performance of $Ti_3C_2T_x$/AlGaN detectors could be adjusted accordingly. The effect of oxidation process of Ti_3C_2Tx on performance of $Ti_3C_2T_x$/AlGaN photodetectors has been investigated systematically. The optimized devices exhibited a rise time of 72 ms and a decay time 30 ms, achieving a responsivity of 3000 mA/W under 270 nm UV light irradiation.

Keywords Photodetector · Schottky diode · Heterostructure · AlGaN · Two-dimensional materials · MXene

Introduction

Currently, ultraviolet (UV) detection technology has become a highly significant research topic. The UV light in the UVC range (200–280 nm) is referred to as solar-blind UV[1], as it is absorbed by ozone, water vapor, and other substances. Consequently, solar-blind UV radiation is virtually absent on the Earth's surface. The solar-blind UV detection technology has shown broad application prospects in numerous areas such as secure communication [2] and ultraviolet astronomy. AlGaN, a ternary alloy material composed of GaN and AlN [3], exhibits material characteristics that lie between the two [4, 5]. The bandgap width of AlGaN can be continuously adjusted between 3.4 and 6.2 eV by varying the proportion of Al composition. The absorption wavelength range covers the solar-blind UV spectrum. In addition, AlGaN possesses several advantages such as high temperature and radiation resistance [6, 7], making it an ideal material for solar-blind UV detectors. However, AlGaN-based photodetectors still face several limitations. For instance, AlGaN material suffers from high defect density and difficulties in p-type doping [8]. While great efforts have been dedicated to address these difficulties, other strategies should also be taken into account for enhancing performance of detectors.

MXene is a typical two-dimensional material composed of several atomic layers of transition metal carbides, nitrides, or carbonitrides, possessing excellent metallic conductivity, flexibility, and transparency [9]. Due to its tunable work function [10] and electronic band structure [11] through artificial design, MXene can be used as a Schottky electrode material [12]. In MXene, each atomic layer is bonded through in-plane covalent bonds, while the interlayer forces are relatively weak. In MXene, each atomic layer is composed of metal carbides or nitride atoms and connected to each other through covalent bonds in the plane. The formation of this covalent bond gives MXene good structural strength and stability [13–15]. Compared to intra layer covalent bonds, the interlayer forces of MXene are relatively weak. Interlayer

✉ Wei Lü
lw771119@hotmail.com

✉ Xiaojuan Sun
sunxj@ciomp.ac.cn

[1] Key Laboratory of Advanced Structural Materials, Ministry of Education & Advanced Institute of Materials Science, Changchun University of Technology, Changchun 130012, People's Republic of China

[2] State Key Laboratory of Luminescence and Applications, Changchun Institute of Optics, Fine Mechanics and Physics, Chinese Academy of Sciences, Changchun 130033, People's Republic of China

forces are typically contributed by interactions such as van der Waals forces and hydrogen bonds. These interactions are relatively weaker than covalent bonds; therefore, layered structures are prone to phenomena such as detachment and insertion of ions under external forces. As a result, when forming heterostructures [16–18] with semiconductors [19, 20], MXene does not introduce defect states, thereby mitigating the Fermi level pinning effect [21]. In addition, the gas sensing mechanism can be modulated by Schottky junctions on two-dimensional materials and semiconductor surfaces [22, 23]. At present, the surface and heterojunction engineering of MXene has been widely used in sensors and other aspects. The rich surface functions of tunable electronic structures of two-dimensional materials have attracted extensive attention [24, 25].

In this work, based on aforementioned discussion, we propose an external modulation method by combining AlGaN with two-dimensional MXene (Ti_3C_2Tx) to construct Ti_3C_2Tx/AlGaN heterostructures. It has been shown that Ti_3C_2Tx undergoes a transition from a metallic material to a semiconductor depending on oxidation, and the performance of $Ti_3C_2T_x$/AlGaN detectors could be adjusted accordingly. The effect of oxidation process of $Ti_3C_2T_x$ on $Ti_3C_2T_x$/AlGaN photodetectors has been investigated systematically. The optimized devices exhibited a rise time of 72 ms and a decay time 30 ms, achieving a responsivity of 3000 mA/W under 270 nm UV light irradiation.

Experimental

Preparation of $Ti_3C_2T_x$

$Ti_3C_2T_x$ was prepared by etching Ti_3AlC_2 in a LiF/HCl system. 0.8 g LiF was dissolved in a 9 M HCl (10 mL) solution. The mixture was continuously stirred for 15 min. Then, 0.5 g of MAX phase Ti_3AlC_2 powder (98%, particle size 200 mesh, purchased from Shanghai Aladdin Bio-Chem Technology Co., Ltd.) was added to the reaction vessel. The mixture was continuously stirred and reacted for 48 h at 40 °C.

Next, the acidic mixture obtained from the reaction was added to dilute HCl (2 M, 10 mL) and centrifuged at 3500 rpm for 1 min for acid washing. This process was repeated to wash away unreacted LiF. The resulting mixture was then repeatedly washed with deionized water and centrifuged until the upper suspension becomes neutral. The bottom precipitate corresponds to the accordion-like multilayered $Ti_3C_2T_x$, which was collected by vacuum filtration. The $Ti_3C_2T_x$ was ultrasonically cleaned for 15 min under an inert gas atmosphere and then centrifuged at 3500 rpm for 30 min.

Preparation of $Ti_3C_2T_x$/AlGaN heterojunction

The $Ti_3C_2T_x$/AlGaN heterojunction devices were fabricated using the drop-casting method. The n-AlGaN sample used in the experiment was grown on a (0001) sapphire substrate by metal–organic chemical vapor deposition (MOCVD). Firstly, the sapphire substrate was treated with hydrogen gas at 1100 °C. Then, a 500-nm AlN buffer layer was grown at 1225 °C. Subsequently, the GaN template layer was grown on the AlN layer, which included AlGaN/AlGaN strain superlattices (SLs) for dislocation filtering. The growth temperature was 1100 °C and the thickness was 140 nm. Finally, a 500-nm intrinsic AlGaN layer and a 500-nm silicon-doped n-AlGaN layer were grown at 1100 °C [26]. The AlGaN composition in terms of Al and Ga components is 0.55:0.45. A masked polyvinyl chloride (PVC) electrostatic film was applied to the surface of the AlGaN substrate. Then, the prepared $Ti_3C_2T_x$ suspension was dropped into the gaps reserved by the mask and allowed to air dry naturally. Afterwards, the PVC mask was removed, and the sample was further dried before depositing silver electrodes on the top. We choose Ag as the contact electrode metal material with n-AlGaN for two reasons; first, Ag work function is 4.26 electron volts (eV), the contact surface of the two will form a barrier, under forward bias, Schottky barrier becomes thinner, promoting carrier (electron) injection from the metal into the N-type semiconductor. The injected electrons increase the concentration of electrons in the N-type semiconductor, thereby reducing the generation of dark current. Ag/AlGaN Schottky junction is used to prevent reverse leakage current and to reduce dark current generation by injecting carriers, which improves response speed and reduces noise level of the device. The energy band diagram of Ag/AlGaN junction is shown in Fig S8. On the other hand, Ag electrode is cheap, so we explore a low-cost method to modify AlGaN surface.

The structure of the $Ti_3C_2T_x$/AlGaN photodetector is shown in Fig. 1a. The size of the active region is 0.5 cm × 0.5 cm, and the area of MXene is 0.25 cm × 0.25 cm. Figure 1b shows the Scanning Electron Microscope (SEM) image of clay-like $Ti_3C_2T_x$, as depicted in the schematic. The particles observed within the layered structure represent partially oxidized TiO_2 particles. As shown in Fig. 1c, the Transmission Electron Microscope (TEM) image and element mapping of the exfoliated layer $Ti_3C_2T_x$ indicated that layered $Ti_3C_2T_x$ was successfully prepared.

Results and discussion

The $Ti_3C_2T_x$ colloidal solution was incubated and continuously stirred in a 60 ℃ environment. As the incubation and stirring process proceeded, oxidation of $Ti_3C_2T_x$ occurred.

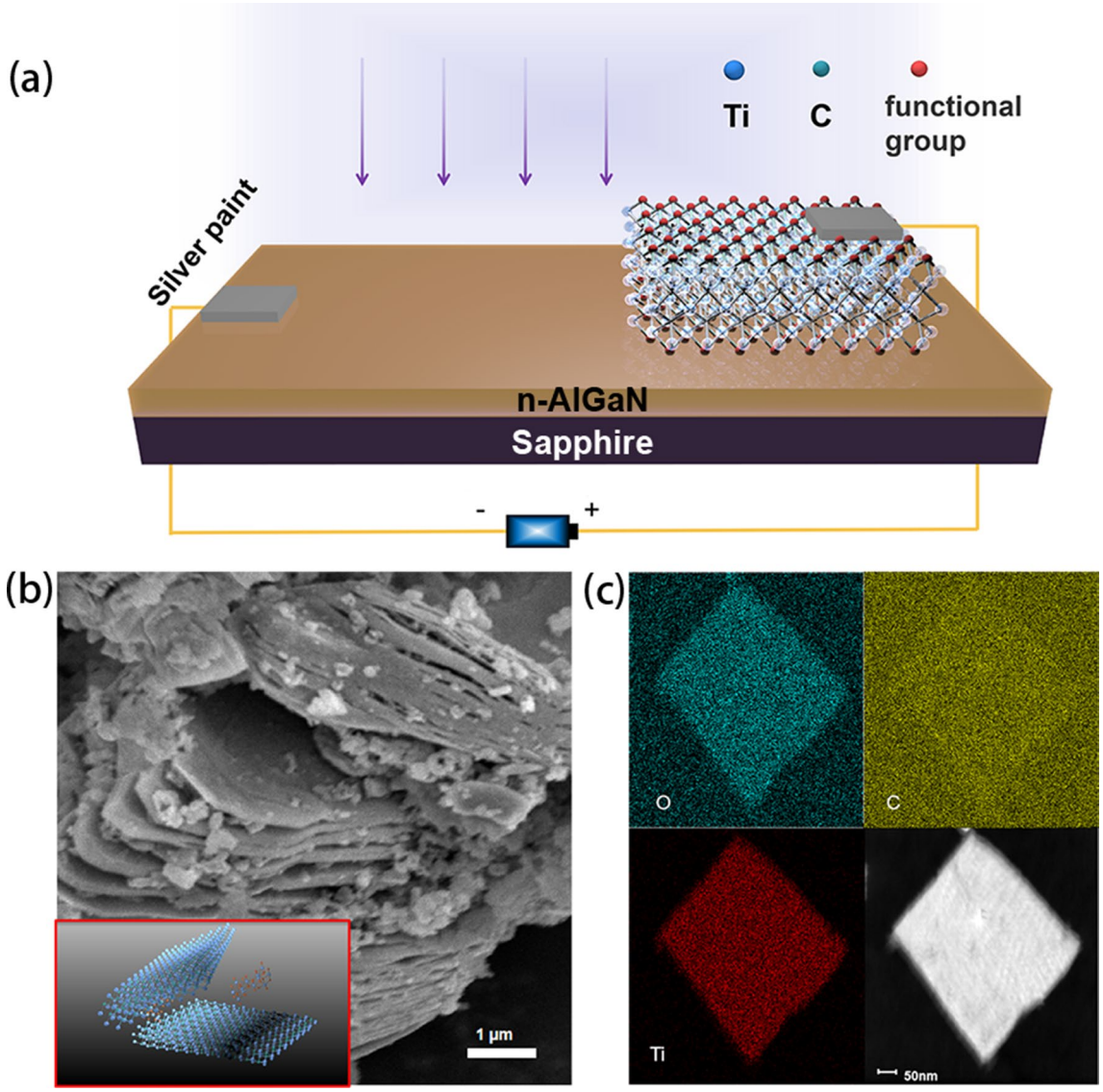

Fig. 1 **a** Schematic diagram of $Ti_3C_2T_x$/AlGaN photodetector structure. **b** SEM image of multilayer $Ti_3C_2T_x$. **c** TEM image and elemental mapping of layered $Ti_3C_2T_x$ after sonication exfoliation

Characterizations were performed on $Ti_3C_2T_x$ samples with different oxidation times. As shown in TEM images in Fig. 2a–c, it can be observed that $Ti_3C_2T_x$ exhibits a distinct layered structure when not subjected to incubation and oxidation. After partial oxidation, TiO_2 nanoparticles present on the surface of the nanosheets. After 120-h oxidation, the nanosheet structure of $Ti_3C_2T_x$ is completely transformed into TiO_2 nanoparticles. This is because during the oxidation process, the surface Ti atoms first combine with O_2 molecules in the environment, and then the intermediate layer Ti atoms diffuse to the outer layer and combine with O_2, causing the layered structure to be completely distorted, resulting in the formation of particulate TiO_2 and carbon substrates with C–C bonds [27, 28]. SEM images in Fig. 2d and e show the $Ti_3C_2T_x$ coated on the surface of AlGaN before and after complete oxidation, respectively. Figures S1 a-b) depict atomic force microscopy images of Ti_3C_2Tx MXene drop casting on silicon wafer surfaces. Before drip casting, Ti_3C_2Tx is sonicated to form a clear layered structure in the image. Figures S2 a-b) show AFM images obtained after 42 h of oxidation with a significant increase in surface titanium dioxide particles. Figure. S3 a-b) show AFM images obtained after 120 h of oxidation where the lamellar structure has been completely lost and the surface appears granular. Different oxidation times of $Ti_3C_2T_x$ were coated on glass substrates, and their crystal structure was characterized by X-ray diffractometer (XRD) in Fig. 2f. After 60-h incubation, peaks corresponding to the anatase and rutile phases of

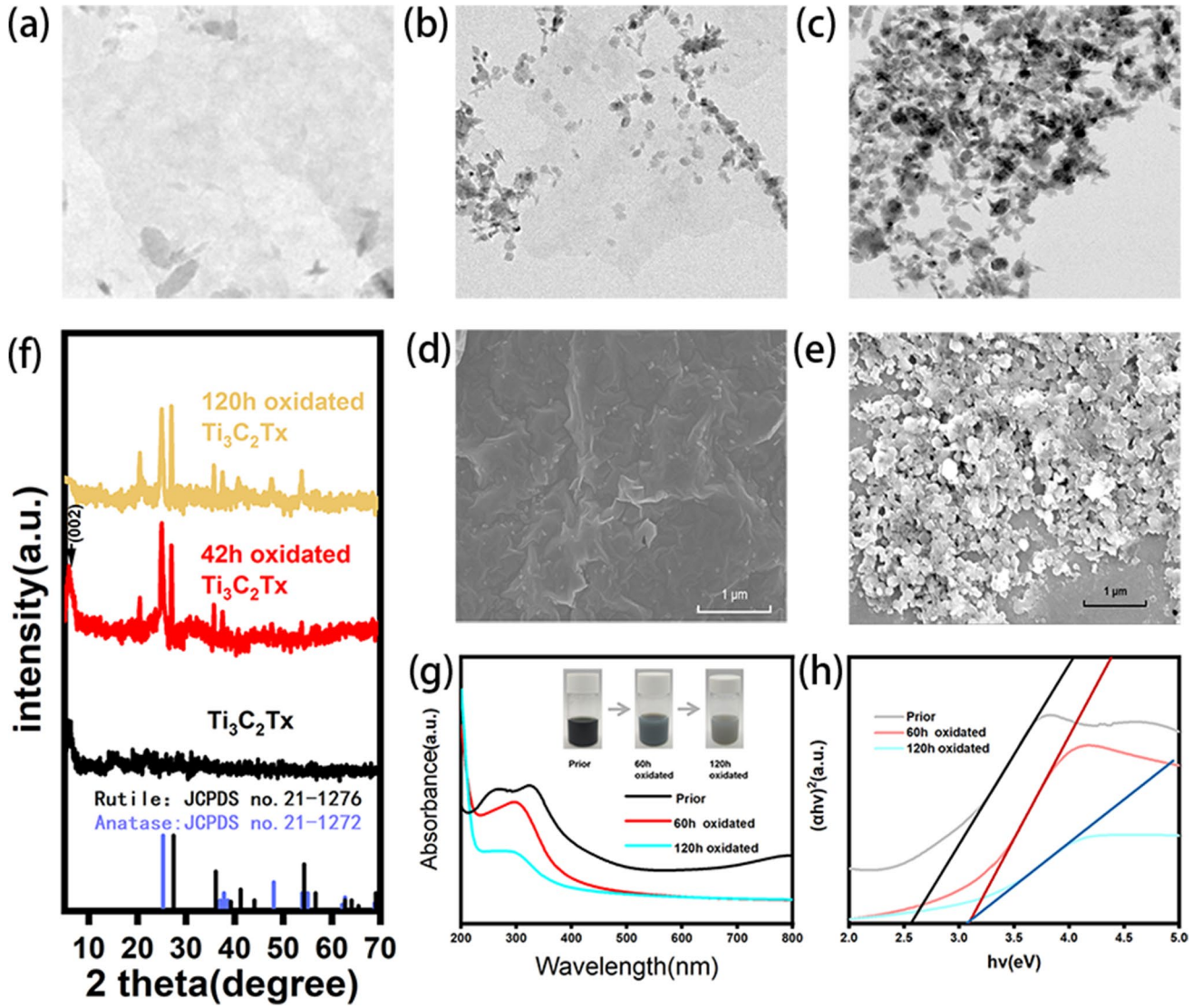

Fig. 2 **a**–**c** TEM images of Ti_3C_2Tx MXene colloidal solution without oxidation, 60-h oxidation, and 120-h oxidation, respectively. **d** SEM image of the detector surface coated with Ti_3C_2Tx without oxidation. **e** SEM image of the detector surface coated with 120 h oxidized Ti_3C_2Tx. **f** XRD patterns of Ti_3C_2Tx MXene at different oxidation degrees. **g** UV–visible absorption spectra of Ti_3C_2Tx e at different oxidation degrees, and the inset is corresponding photos. **h** Optical bandgaps of Ti_3C_2Tx at different oxidation levels

TiO_2 are observed in the XRD spectrum, indicating partial oxidation. After 120-h incubation, there is a significant oxidation of MXene as evidenced by the disappearance of the (002) peak, while the peaks corresponding to the anatase and rutile phases of TiO_2 remain. The TEM images and XRD patterns are highly correlated, providing evidence that as the oxidation of $Ti_3C_2T_x$ progresses, the nanosheets gradually transform into TiO_2 nanoparticles. This is also verified by the UV–Vis absorption spectra. Figure 2g displays the UV–Vis absorption spectra of $Ti_3C_2T_x$ at various oxidation degrees, with the corresponding samples shown in the inset [29, 30]. The MXene colloid solution appears dark black without incubation and oxidation. After 60-h oxidation, partial oxidation of $Ti_3C_2T_x$ occurs, resulting in a lighter color. After 120-h oxidation, most of the $Ti_3C_2T_x$ has been oxidized, and the colloid solution turns gray. The optical bandgap of $Ti_3C_2T_x$ is further analyzed using UV–Vis absorption spectroscopy, as shown in Fig. 2h. The optical bandgap of $Ti_3C_2T_x$ was estimated to be highly consistent after moderate and complete oxidation, with Eg ~ 3.1 eV.

To validate the metallic properties of Ti_3C_2Tx, we spin-coated non-oxidized Ti_3C_2Tx onto a glass substrate and deposited Ag electrodes on one end. Linear sweep voltammetry (LSV) curves were measured, as shown in Fig. 3a. The LSV curve of Ti_3C_2Tx with Ag exhibits a clear linear relationship, indicating the metallic characteristics of non-oxidized MXene. The optoelectronic characteristics of the device were measured in both dark and under 270 nm

ultraviolet light. The device exhibits distinct rectification characteristics, indicating that it is a well-performing diode-like structure. Under UV light irradiation, the I-V values of the device are higher than those under dark conditions, demonstrating its high sensitivity to UV light.

In the Ti_3C_2Tx/AlGaN heterojunction, Ti_3C_2Tx not only forms a Schottky contact with AlGaN, but also serves as a transparent layer and a conductive layer [31, 32]. In order to investigate the effect of oxidation degree of Ti_3C_2Tx on the photodetection performance of the device, Ti_3C_2Tx with varying oxidation times was spin-coated onto the surface of AlGaN. Figure S4 shows the light–dark current curves of Ti_3C_2Tx MXene/n-AlGaN photodetectors with different oxidation times. Photocurrent variation trend of Ti_3C_2 Tx MXene/n-AlGaN photodetector with different oxidation time (logarithmic function coordinate) is shown in Figure S5. As shown in Fig. 3b and c, the photocurrent keeps increasing in the range of 0 to 42-h oxidation. After 42 h, both the photocurrent and dark current gradually decrease with further increase in oxidation time, ultimately reaching a stable state after 120 h without any further changes. This indicates that the resistance of the Ti_3C_2Tx/AlGaN device decreases initially and then increases as the oxidation degree of the Ti_3C_2Tx surface deepens. Figure 3d shows the photocurrent-to-dark current ratio of the device after 120 h of oxidation, with a light source of 270 nm ultraviolet light and an intensity of 3.5 mW/cm^2. The responsivity curve of Ti_3C_2Tx MXene/n-AlGaN photodetectors after 120-h oxidation measured at different wavelengths is shown in Figure S5. Figure 3e depicts the I-V curves of the device at different oxidation times plotted on a logarithmic scale. As shown in Fig. 3f, the photodetection response of the device also initially increases and then decreases with oxidation time, reaching its peak at 42 h.

Since 42-h oxidization achieved the best performance, the Ti_3C_2Tx/AlGaN photodiode fabricated based on 42 h oxidized Ti_3C_2Tx is used for further investigation. The I-T curves of the Ti_3C_2Tx/AlGaN photodiode under different UV light powers at a bias voltage of 2 V are shown in Fig. 4a. When the device is subjected to UV light, the photoelectric current rapidly increases and reaches its maximum. When the UV light is turned off, the current drops sharply. Response time is also an important parameter in the performance of a photodetector. The rise time Tr of the photodetector device is defined as the time required for the photoelectric current to rise from 10% of the dark current to 90% of the photoelectric current. Conversely, the recovery time Td is defined as the time required for the photoelectric

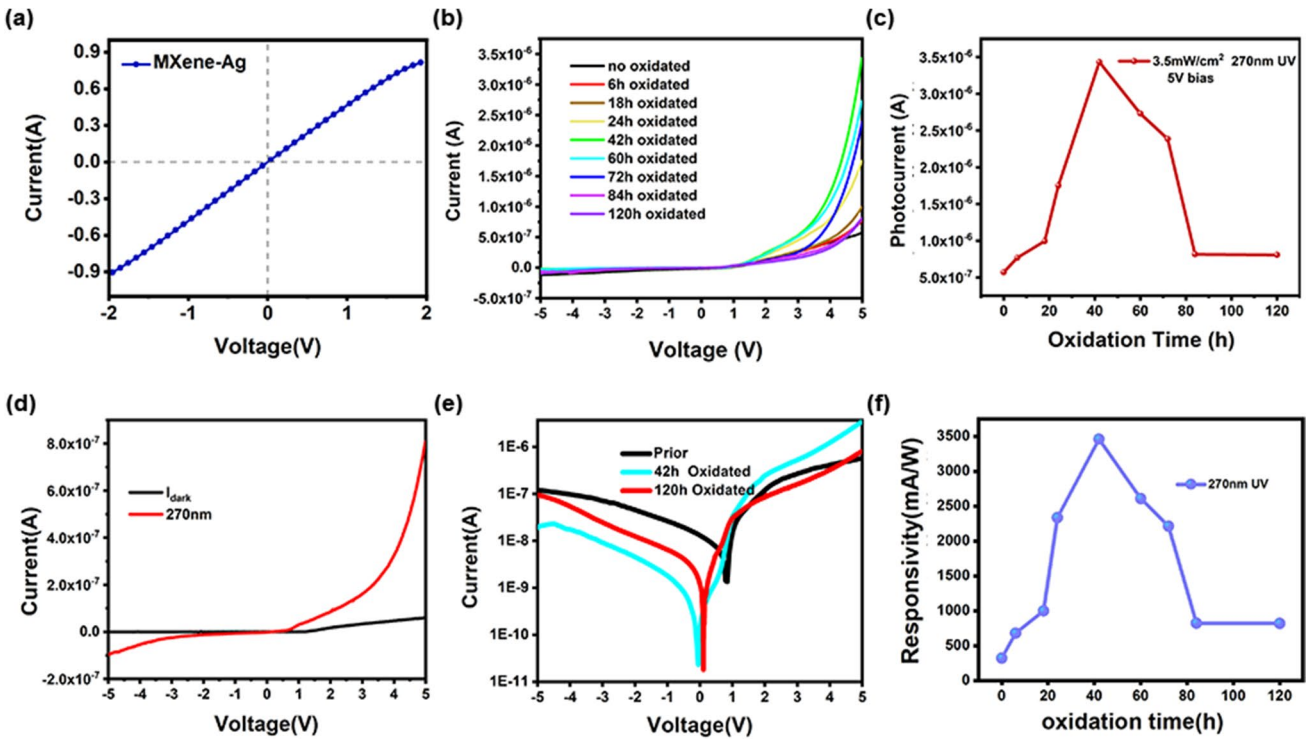

Fig. 3 **a** The Ag/Ti_3C_2Tx Ohmic contact exhibits linear I-V characteristics. **b** The I-V curves of the photodetector under illumination at a wavelength of 270 nm and a light power of 3.5 mW/cm^2 for oxidation times ranging from 0 to 120 h. **c** The photocurrent trend of the photodetector under the illumination of 3.5 mW/cm^2 and 270 nm wavelength with 5 V bias voltage applied. **d** The I-V curves of the photodetector for the cases of 120-h oxidation. **e** The logarithmic I-V curves of the photodetector's photocurrent for different oxidation times. **f** The photodetector's photodetection response at different oxidation times

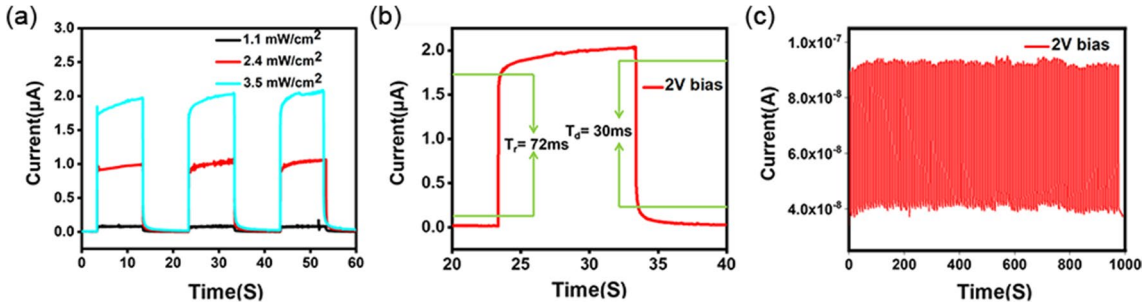

Fig. 4 **a** The i-t characteristics of the photodetector under different light power densities and 2 V bias. **b** The single cycle of the i-t curve. **c** The i-t curve of 100 cycles

current to drop from 90 to 10% of the dark current. As shown in Fig. 4b, by enlarging one response cycle in the I-T curve of the device, we can determine the rise/recovery time of the device. It was found that the rise time is 72 ms and the recovery time is 30 ms. As shown in Fig. 4c, after 100 cycles, the photodetection performance remained stable.

An explanation for the potential mechanism of the Ti_3C_2Tx/AlGaN photodetector is proposed. The energy band diagram of the Ti_3C_2Tx/AlGaN interface is shown in Fig. 5. As a metal carbide, Ti_3C_2Tx can form a Schottky contact with n-AlGaN. AlGaN material is a ternary alloy of GaN and AlN, and its bandgap varies with the change of Al composition. The bandgap can be estimated by the following formula [26]:

$$E_g^{AlGaN} = xE_g^{AlN} + (1-x)E_g^{GaN} - bx(1-x) \quad (1)$$

Here, x represents the Al composition in AlGaN. Eg^{AlGaN}, Eg^{GaN}, and Eg^{AlN} represent the bandgap widths of AlGaN, GaN, and AlN, respectively. b is the curvature factor, which was experimentally determined to be 1 eV. In this experiment, n-doped $Al_{0.55}Ga_{0.45}N$ was used, with a bandgap of 4.59 eV. When Ti_3C_2Tx is not oxidized, its work function is 5.35 eV [33]. Experimental calculations indicate that after

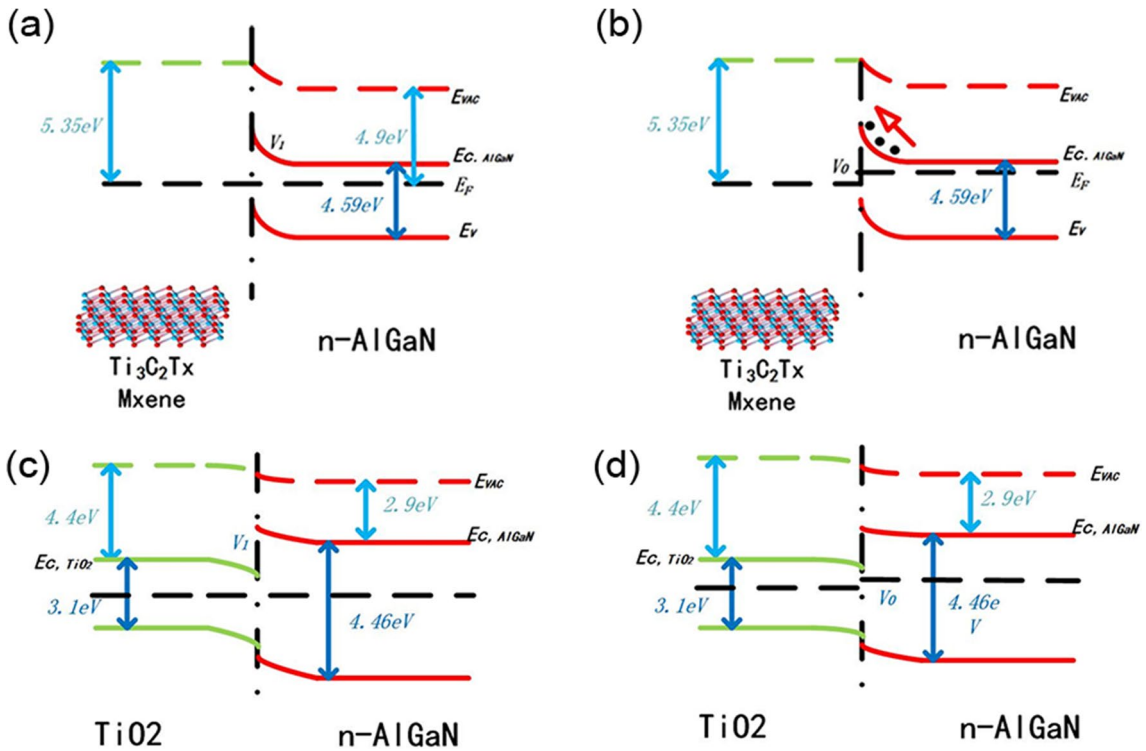

Fig. 5 Band diagrams of the Ti_3C_2Tx/AlGaN device. **a**, **b** Band diagrams of Ti_3C_2Tx/n-AlGaN Schottky junction in equilibrium and under UV light illumination. **c**, **d** Band diagrams of TiO_2/n-AlGaN heterojunction in equilibrium and under applied forward bias voltage

complete oxidation, Ti_3C_2Tx exhibits semiconductor properties with a bandgap of 3.1 eV.

When the Ti_3C_2Tx/n-AlGaN heterojunction structure is in equilibrium, the band diagram of the Ti_3C_2Tx/n-AlGaN Schottky junction is shown in Fig. 5a. The work function of Ti_3C_2Tx is 5.35 eV. In the Ti_3C_2Tx/n-AlGaN heterojunction structure, electrons will flow from heavily doped n-AlGaN to Ti_3C_2Tx, generating a depletion layer and establishing an internal built-in potential V_1. When the device is under ultraviolet illumination, as shown in Fig. 5b, electrons absorb the energy from photons and transition to the conduction band, resulting in an increase in the Fermi level and the generation of the built-in potential V_0. Consequently, the internal potential V_1 is weakened by the photogenerated potential V_0, resulting in a difference of $q(V_1\text{-}V_0)$ between the Fermi levels of Ti_3C_2Tx and n-AlGaN under ultraviolet illumination. Therefore, this would reduce V_{bi} and would facilitate electron current from AlGaN to MXene. This photoexcitation process leads to an increase in the electron concentration in the conduction band, thereby enhancing the responsiveness of the photodetector[34].

Figure 5c illustrates the band diagrams of n-AlGaN and TiO_2 under equilibrium conditions and under forward bias. TiO_2 exhibits non-stoichiometric defects where the chemical formula can be written as TiO_2-x. In this case, Ti^{3+} replaces Ti^{4+} resulting in oxygen vacancies, causing the electron concentration to be higher than the hole concentration in the charge carriers [35]. The schematic diagram of the energy bands before and after contact between TiO_2 and n-AlGaN, as well as after applying bias voltage, is shown in Fig. S7. This macroscopically manifests as n-type doping, leading to the formation of a heterojunction with n-AlGaN. After complete oxidation of Ti_3C_2Tx to TiO_2, the conduction band and valence band of TiO_2 are located at − 4.40 eV and − 7.50 eV, respectively. The n-type behavior of both materials has been confirmed through Hall effect measurements. The Hall effect measurement of n-AlGaN indicates a charge carrier density on the order of $10^{17}/cm^3$, while the TiO_2 film formed from the oxidation of Ti_3C_2Tx exhibits a charge carrier density on the order of $10^{11}/cm^3$. Due to the higher electron density on the n-AlGaN side compared to the TiO_2 side, electrons will diffuse from the AlGaN thin film to the TiO_2 side until the Fermi level aligns. This results in the formation of an electron depletion region on the AlGaN side and an electron accumulation region on the TiO_2 side. The neutral depletion width formed by the electron depletion region and electron accumulation region contributes to the formation of the built-in potential V_1 for charge carrier transport, as depicted in Fig. 5d. When a forward bias is applied to both ends of the n–n heterojunction relative to TiO_2, electrons are injected from the TiO_2 side to the AlGaN side due to drift current. As a result, the height of the barrier decreases by eV_0. This causes a decrease in the height of the barrier by eV_0.

Ti_3C_2Tx is a material with metallic properties, and its work function is approximately − 5.35 eV. When Ti_3C_2Tx undergoes partial oxidation, the resulting TiO_2 has an increased work function. As a result, the built-in potential of the Ti_3C_2Tx/AlGaN interface increases, causing the depletion layer to widen. This widening of the depletion layer is beneficial for electron transport [36–38]. Simultaneously, compared to the unoxidized and fully layered Ti_3C_2Tx, the presence of TiO_2 causes an expansion of the interlayer spacing in the Ti_3C_2Tx film, making the film surface more uniform and increasing the specific surface area. The TiO_2/Ti_3C_2Tx structure provides channels for ion/electron transport, resulting in increased current in the device during partial oxidation of Ti_3C_2Tx. As the oxidation time increases, Ti_3C_2Tx is completely oxidized, with most of its two-dimensional structure replaced by TiO_2 nanoparticles. Its metallic properties are completely lost, and the single-layer structure deteriorates, leading to a decrease in conductivity and a reduction in current in the device.

Conclusion

In summary, we have prepared the layered Ti_3C_2Tx material using an etching method, and a Ti_3C_2Tx/n-AlGaN photodiode structure for photodetection was fabricated using a simple drop-casting method. The Schottky junction formed in this structure effectively enhances the device's photoresponsiveness. As Ti_3C_2Tx gradually oxidizes to TiO_2 in the air, the photodetector exhibits an initial increase followed by a decrease in its photoresponse. However, when Ti_3C_2Tx is highly oxidized, it almost completely loses its layered structure and undergoes a transition from metal to semiconductor properties, resulting in decreased conductivity and degraded device performance. This work provides a certain experimental foundation for the subsequent construction of TiO_2/Ti_3C_2Tx hybrid heterojunction photodetectors. The research findings suggest that the oxidation of Ti_3C_2Tx improves its energy level alignment with AlGaN, leading to suppressed carrier recombination. However, deep oxidation results in the loss of its layered structure, leading to a gradual decrease in the device's photoresponse. This work provides a foundation for future development of TiO_2/Ti_3C_2Tx hybrid heterostructure photodetectors. By controlling the degree of oxidation of MXene, it is possible to maximize the advantages of two-dimensional layered materials for designing more efficient day-blind photodetectors.

Supplementary Information The online version contains supplementary material available at https://doi.org/10.1007/s11581-023-05362-8.

Author contribution Jingzhao Yü: writing—original draft (equal), investigation (equal), data curation (equal). Yuqing Zhang: investigation (equal), data curation (equal). Liying Wang: formal analysis

(equal). Xijia Yang: resources. Yue Yang: data curation (equal). Ke Jiang: methodology (equal); conceptualization (equal). Wei Lü: funding acquisition (equal), project administration (equal). Xiaojuan Sun: resources (equal).

Funding This work was supported by the National Key R&D Program of China (Grant No. 2022YFB3604903), the National Natural Science Foundation of China (62121005, 62004196, 61827813), the Natural Science Foundation of Jilin Province (20230101345JC, 20230101360JC), and the Department of Science and Technology of Jilin Province (20220101235JC, 20210101077JC, YDZJ202201ZYTS361).

Data availability The data that support the findings of this study are available from the corresponding author upon reasonable request.

Declarations

Competing interests The authors declare no competing interests.

References

1. Cai Q, You H, Guo H, Wang J, Liu B, Xie Z, Chen D, Lu H, Zheng Y, Zhang R (2021) Progress on AlGaN-based solar-blind ultraviolet photodetectors and focal plane arrays. Light Sci Appl 10:94
2. Chong H, Wei G, Hou H, Yang H, Shang M, Gao F, Yang W, Shen G (2015) High-performance solar-blind ultraviolet photodetector based on electrospun TiO_2-$ZnTiO_3$ heterojunction nanowires. Nano Res 8:2822–2832
3. Zhang H, Huang C, Song K, Yu H, Xing C, Wang D, Liu Z, Sun H (2021) Compositionally graded III-nitride alloys: building blocks for efficient ultraviolet optoelectronics and power electronics. Rep Prog Phys 84. https://doi.org/10.1088/1361-6633/abde93
4. Pandit B, Cho J (2021) Solar-blind ultraviolet photodetectors with thermally reduced graphene oxide formed on high-Al-content AlGaN layers. AIP Adv 11:115322
5. Pandit B, Jang HS, Jeong Y, An S, Chandramohan S, Min KK, Won SM, Choi CJ, Cho J, Hong S, Heo K (2023) Highly sensitive ultraviolet photodetector based on an AlGaN/GaN HEMT with graphene-On-p-GaN mesa structure. Adv Mater Interfaces 10. https://doi.org/10.1002/admi.202202379
6. Pandit B, Cho J (2018) AlGaN ultraviolet metal–semiconductor–metal photodetectors with reduced graphene oxide contacts. Appl Sci 8:2098
7. Pandit B, Schubert EF, Cho J (2020) Sci Rep 10(1):22059
8. Jiang K, Sun X, Ben J, Jia Y, Liu H, Wang Y, Wu Y, Kai C, Li D (2018) The defect evolution in homoepitaxial AlN layers grown by high-temperature metal–organic chemical vapor deposition. CrystEngComm 20:2720–2728
9. Wei Y, Zhang P, Soomro RA, Zhu Q, Xu B (2021) Advances in the synthesis of 2D MXenes. Adv Mater 33:e2103148
10. Vida J, Gemeiner P, Pavlickova M, Mazalova M, Soucek P, Plasienka D, Homola T (2023) Nanocrystalline TiO(2)/Ti(3)C(2)T(x) MXene composites with a tunable work function prepared using atmospheric pressure oxygen plasma. Nanoscale 15:1289–1298
11. Neupane GP, Yildirim T, Zhang L, Lu Y (2020) Retracted: emerging 2D MXene/organic heterostructures for future nanodevices. Adv Funct Mater 30. https://doi.org/10.1002/adfm.202005238
12. Wang C, Xu X, Tyagi S, Rout PC, Schwingenschlogl U, Sarkar B, Khandelwal V, Liu X, Gao L, Hedhili MN, Alshareef HN, Li X (2023) Ti(3) C(2) T(x) MXene van der Waals Gate Contact for GaN High Electron Mobility Transistors. Adv Mater 35:e2211738
13. Feng A, Yu Y, Mi L, Yu Y, Song L (2018) Comparative study on electrosorptive behavior of NH_4HF_2-etched Ti_3C_2 and HF-etched Ti_3C_2 for capacitive deionization. Ionics 25:727–735
14. Y Xie, X Xiong , K Han (2021) Ionics 27 (8) 3373-3382
15. Qi J, Gu H, Ruan C, Zhu L, Meng Q, Sui Y, Feng X, Wei W, Zhang H (2022) Ionics 28(6):2979–2989
16. Montazeri K, Currie M, Barsoum MW, Nabet B (2022) Ultra-high speed, high-sensitivity spin-cast MXene-semiconductor-MXene photodetectors. Adv Funct Mater 32. https://doi.org/10.1002/adfm.202206942
17. Zhang Z, Lin P, Liao Q, Kang Z, Si H, Zhang Y (2019) Graphene-based mixed-dimensional van der Waals heterostructures for advanced optoelectronics. Adv Mater 31:e1806411
18. Jariwala D, Marks TJ, Hersam MC (2017) Mixed-dimensional van der Waals heterostructures. Nat Mater 16:170–181
19. Song W, Liu Q, Chen J, Chen Z, He X, Zeng Q, Li S, He L, Chen Z, Fang X (2021) Interface Engineering Ti(3) C(2) MXene/silicon self-powered photodetectors with high responsivity and detectivity for weak light applications. Small 17:e2100439
20. Luo L, Huang Y, Cheng K, Alhassan A, Alqahtani M, Tang L, Wang Z, Wu J (2021) MXene-GaN van der Waals metal-semiconductor junctions for high performance multiple quantum well photodetectors. Light Sci Appl 10:177
21. Prabaswara A, Kim H, Min JW, Subedi RC, Anjum DH, Davaasuren B, Moore K, Conroy M, Mitra S, Roqan IS, Ng TK, Alshareef HN, Ooi BS (2020) Titanium carbide MXene nucleation layer for epitaxial growth of high-quality GaN nanowires on amorphous substrates. ACS Nano 14:2202–2211
22. Luo G, Zhang Z, Wang J, Huang M, Long Y, Liu Y, Zeng Z, Wang Y, Zou J, Ren A, Luo S, Yang Y, Li W, Lin H, Zhao D (2023) High-performance ultraviolet photodetectors enabled by van der Waals Schottky junction based on TiO_2 nanorod arrays/Au-modulated Ti_3C2Tx MXene. Adv Funct Mater 33. https://doi.org/10.1002/adfm.202211610
23. Hu C, Du Z, Wei Z, Li L, Shen G (2023) Functionalized Ti_3C_2Tx MXene with layer-dependent band gap for flexible NIR photodetectors. Appl Phys Rev 10. https://doi.org/10.1063/5.0140861
24. Reddy MSB, Aich S (2024) Recent progress in surface and heterointerface engineering of 2D MXenes for gas sensing applications. Coord Chem Rev 500. https://doi.org/10.1016/j.ccr.2023.215542
25. Choi J, Kim YJ, Cho SY, Park K, Kang H, Kim SJ, Jung HT (2020) In situ formation of multiple Schottky barriers in a Ti_3C_2 MXene film and its application in highly sensitive gas sensors. Adv Funct Mater 30. https://doi.org/10.1002/adfm.202003998
26. Li D, Jiang K, Sun X, Guo C (2018) AlGaN photonics: recent advances in materials and ultraviolet devices. Adv Opt Photonics 10:43–110
27. Lotfi R, Naguib M, Yilmaz DE, Nanda J, van Duin ACT (2018) A comparative study on the oxidation of two-dimensional Ti_3C_2MXene structures in different environments. J Mater Chem A 6:12733–12743
28. Chae Y, Kim SJ, Cho SY, Choi J, Maleski K, Lee BJ, Jung HT, Gogotsi Y, Lee Y, Ahn CW (2019) An investigation into the factors governing the oxidation of two-dimensional Ti(3)C(2) MXene. Nanoscale 11:8387–8393
29. Numan A, Rafique S, Khalid M, Zaharin HA, Radwan A, Mokri NA, Ching OP, Walvekar R (2022) Microwave-assisted rapid MAX phase etching and delamination: a paradigm shift in MXene synthesis. Mater Chem Phys 288. https://doi.org/10.1016/j.matchemphys.2022.126429
30. Berdiyorov GR (2016) Optical properties of functionalized $Ti_3C_2T_2$ (T = F, O, OH) MXene: first-principles calculations. AIP Advances 6. https://doi.org/10.1063/1.4948799

31. H. Xu, A. Ren, J. Wu, Z. Wang, Recent advances in 2D MXenes for photodetection, Advanced Functional Materials, 30 (2020).
32. Liu N, Yu L, Liu B, Yu F, Li L, Xiao Y, Yang J, Ma J (2023) Ti(3) C(2) -MXene partially derived hierarchical 1D/2D TiO_2 / Ti_3C_2 heterostructure electrode for high-performance capacitive deionization. Adv Sci (Weinh) 10:e2204041
33. Yang L, Kan D, Dall'Agnese C, Dall'Agnese Y, Wang B, Jena AK, Wei Y, Chen G, Wang X-F, Gogotsi Y, Miyasaka T (2021) Performance improvement of MXene-based perovskite solar cells upon property transition from metallic to semiconductive by oxidation of Ti_3C_2Txin air. J Mater Chem A 9:5016–5025
34. Ozel K, Yildiz A (2021) High-detectivity ultraviolet-B photodetector based on SnO_2 thin film/Si heterojunction. Semicond Sci Technol 36:095001
35. Han X, Amrane N, Zhang Z, Benkraouda M (2019) Insights into the characteristic gap level and n-type conductivity of rutile TiO_2 from the hybrid functional method. J Phys Chem C 123:2037–2047
36. Zhang H, Zhang X, Xie C, Shi W, Yang P (2023) Composite nanoarchitectonics with TiO(2) nanocrystals and superior thin Ti(3) C(2)T(x) nanosheets towards efficient NO removal. Environ Res 227:115793
37. Luo G, Zhang Z, Wang Y, Deng Q, Pan S, Wang T, Li Q, Liu K, Kong P, Zhang J, Luo S, Lin H (2023) A self-powered ultraviolet photodetector with van der Waals Schottky junction based on TiO_2 nanorod arrays/Au-modulated V_2CT MXene. J Mater Sci Technol 156:83–91
38. Yuan Z, Fan Y, Chen Y, Liu X, Liu B, Han S (2020) Two-dimensional C@TiO_2/Ti_3C_2 composite with superior catalytic performance for $NaAlH_4$. Int J Hydrogen Energy 45:21666–21675